X-ray diagnostics for the cavity-based x-ray free-electron laser project

Peifan Liu,[1] Paresh Pradhan,[1] Antonino Miceli,[1] Donald A. Walko,[1] Deming Shu,[1]
Joseph Sullivan,[1] Keenan Lang,[1] Mark Rivers,[2] Mario Balcazar,[3] Kenan Li,[3]
Rachel Margraf,[3] Aliaksei Halavanau,[3] Anne Sakdinawat,[3] Takahiro Sato,[3]
Diling Zhu,[3] and Yuri Shvyd'ko[1,*]

[1]*Advanced Photon Source, Argonne National Laboratory, Lemont, Illinois 60439, USA*
[2]*Center for Advanced Radiation Sources, The University of Chicago, Argonne, Illinois 60439, USA*
[3]*SLAC National Accelerator Laboratory, Menlo Park, California 94025, USA*

(Received 29 April 2024; accepted 27 August 2024; published 4 November 2024)

The success of x-ray free-electron lasers (XFELs) in recent years has greatly advanced many scientific fields. However, most of these XFELs suffer from a low longitudinal coherence and instabilities due to the stochastic start-up process. A cavity-based x-ray free-electron laser (CBXFEL) is a possible future direction in the development of fully coherent and stable x-ray sources. One of the challenges of a CBXFEL is the requirement for the μm-sized electron bunches to fully overlap in three dimensions with the circulating μm-sized x-ray pulses in an x-ray cavity tens or hundreds of meters long. We present here the development of an x-ray diagnostics system for accurate alignment of x-ray beams in the CBXFEL cavity. The system was developed within the framework of a CBXFEL research and development collaboration among Argonne National Laboratory, SLAC National Accelerator Laboratory, and Spring-8. All the designed diagnostic components have been fully characterized at the Advanced Photon Source to demonstrate a capability for sub-μrad angular and μm spatial alignment of the CBXFEL cavity.

DOI: 10.1103/PhysRevAccelBeams.27.110701

I. INTRODUCTION

In the last two decades, the successful operation of single-pass x-ray free-electron lasers (FELs) with extreme brightness, transverse coherence, and ultrashort pulse length [1–4] has paved the way for diverse science applications ranging from investigation of femtosecond dynamics of atomic and molecular systems [5,6] to long-lived, ultra-narrow nuclear resonances [7]. However, such x-ray FEL (XFEL) pulses, mostly based on the self-amplified spontaneous emission (SASE) that arises from the incoherent shot noise, usually have poor longitudinal coherence.

Along with different self-seeding schemes to improve the longitudinal coherence of SASE XFEL pulses [2,8–12], the cavity-based x-ray free-electron laser (CBXFEL), such as a low-gain x-ray FEL oscillator (XFELO) [13–15] or a high-gain x-ray regenerative amplifier FEL (XRAFEL) [16–18], is a promising candidate for producing high-brilliance x-rays with full coherence and good stability. With the x-ray feedback from a narrow-band x-ray cavity, the CBXFEL pulse is expected to have full coherence and a narrow energy bandwidth, which can be as small as a few meV for an XFELO [13,14].

CBXFELs are built upon repeated FEL interactions between electron pulses and circulating x-ray pulses in an x-ray cavity. The cavity consists of Bragg-reflecting diamond crystal mirrors with narrow bandwidth and near 100% x-ray reflectivity, along with aberration-free focusing elements. One of the practical challenges of a CBXFEL is the requirement of three-dimensional synchronization or overlapping between the electron and x-ray pulses. The challenge arises because the round-trip length through the x-ray cavity is usually tens or hundreds of meters and the electron and x-ray pulses usually have a length and transverse size in the range of a few tens of microns (see Table I). As a result, all cavity optical components must be aligned with a μrad or even nrad angular and a μm spatial precision to ensure that the to-be-amplified x-ray beam meets a fresh electron bunch after traveling tens to hundreds of meters in the cavity and returning into the undulators [19].

Here, we report on the design, manufacturing, and characterization of x-ray diagnostic components for precise alignment and characterization of a CBXFEL x-ray cavity. This work was performed within the framework of a research and development (R&D) collaboration among Argonne National Laboratory (ANL), SLAC National Accelerator Laboratory (SLAC), and Spring-8 [20]. A schematic of the CBXFEL layout is shown in Fig. 1.

---

[*] Contact author: shvydko@anl.gov

TABLE I. Parameters of the electron and FEL pulses in the CBXFEL project.

Electron beam	
Energy	10.7 GeV
Bunch length	50^{a}–300^{b} fs (15–90 μm)
Root-mean-square beam size	22–24 μm
Two-bunch separation	~218 ns (65.5 m)
FEL pulse	
Energy	9.831 keV
Bunch length	$\sim 25^{a}$–1000^{b} fs (7.5–300 μm)
Waist size	~32 μm
Rayleigh range	~26 m

[a] In high-gain XRAFEL scheme.
[b] In low-gain XFELO scheme.

The CBXFEL is driven by a pulsed electron beam propagating through an undulator cascade which provides FEL gain. A rectangular x-ray cavity monochromatizes and circulates the x-ray pulses to promote repeated FEL interactions with electron pulses. The main physical parameters of the electron and x-ray pulses are listed in Table I. The electron pulses are delivered in pairs (separated by 218 ns) from the Linac Coherent Light Source II (LCLS-II) copper linac at a 120 Hz repetition rate [21,22]. The rectangular x-ray cavity consists of four diamond crystal mirrors C_1–C_4, which reflect 9.831-keV x-rays in the 400 Bragg reflection exactly at 45° with high reflectivity and within a narrow energy bandwidth of ~90 meV. The cavity also contains two refractive lenses L_1 and L_2, which are required for x-ray beam shaping and mode control. The detailed optical design of the x-ray cavity is discussed in a separate publication [23,24].

For this R&D project, the goal is to measure the cavity ringdown and two-pass gain in both low-gain XFELO and high-gain XRAFEL schemes. To achieve this goal, different types of x-ray diagnostic elements are required: x-ray beam position and profile monitors (XBPMs), x-ray beam intensity monitors (XBIMs), and a meV-resolution x-ray spectrograph. These diagnostic components are designed to ensure that the x-rays are circulating in a closed orbit and that the recirculating x-ray pulses and the electron pulse overlap in three dimensions. They will be installed both inside and outside the CBXFEL cavity to ensure the accuracy of the initial and final (fine) beam alignment and to characterize and optimize the FEL performance.

II. DIAGNOSTICS OVERVIEW FOR THE CAVITY-BASED FREE-ELECTRON LASER (CBXFEL) PROJECT

Achieving three-dimensional overlapping of the electron and photon pulses requires alignment with sub-μrad angular and μm spatial accuracy due to the long cavity (65.5-m round-trip length) and small electron and photon beam size (see Table I). To achieve this alignment accuracy, different types of XBPMs and XBIMs and a meV-resolution x-ray spectrograph have been designed [28]. They will be installed in seven different stations (stations A–G), as shown in Fig. 1. Stations A–F are installed in the undulator tunnel, and station G is located about 250 m downstream of the undulators.

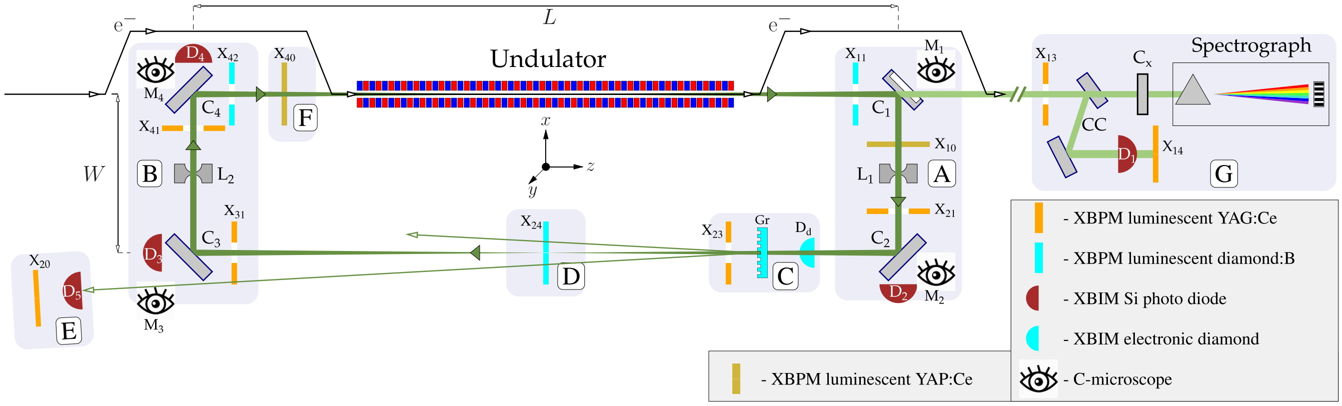

FIG. 1. Overview of experimental setup and diagnostics for the cavity-based x-ray free-electron laser (CBXFEL) project. The CBXFEL consists of an electron beam source, a cascade of undulators, and an x-ray cavity. The rectangular x-ray cavity consists of four diamond crystal mirrors (C_1–C_4) reflecting x-rays in the 400 Bragg reflection exactly at 45° with a photon energy of 9.831 keV and two x-ray lenses (L_1–L_2) in stations A and B. Drumhead crystal [23,25] C_1, with a ~20 μm thin membrane, is used for x-ray output coupling [13,14,26]. The long-arm length L of the rectangle is 32.10 m, and the short-arm length W is 0.65 m. Different types of diagnostics have been designed to be installed in stations A, B, C, D, E, F, and G: x-ray beam position/profile monitors (XBPMs) X_{11}–X_{40} and M_1–M_4; x-ray beam intensity monitors (XBIMs) D_1–D_5 and D_d; and a meV-resolution hard x-ray spectrograph. A diamond crystal C_x in the 440 exact Bragg back-reflection at 9.831 keV is used for accurate photon energy calibration and for angular alignment of crystal C_1. A diamond grating Gr [27] downstream of crystal C_2 in station C and associated diagnostics in station E are used for alternative output coupling and x-ray characterization.

TABLE II. Simulated photon flux values per single pulse or per second (assuming 120-Hz repetition rate) for the CBXFEL R&D project in both XFELO and XRAFEL schemes [32]. The diagnostic components are designed to be sensitive to an average photon flux of a monochromatic beam in the XRAFEL mode (highlighted).

		XFELO		XRAFEL	
Type	Unit	First pulse	Second pulse	First pulse[a]	Second pulse
Average photons per pulse, total	(ph/pulse)	5×10^7	5×10^7	7.4×10^7	2.2×10^8
Average photons per pulse, monochromatic	(ph/pulse/100 meV)	5×10^4	1×10^{5}[b]	3.0×10^{5}[b]	1.2×10^7
Average flux, total	(ph/s)	6×10^9	6×10^9	8.9×10^9	2.6×10^{10}
Average flux, monochromatic	(ph/s/100 meV)	6×10^6	1.2×10^7	$\mathbf{3.6 \times 10^7}$	1.4×10^9

[a] Experimentally measured values for 30-fs, 4-kA e-beam at the LCLS.
[b] Subject to strong shot-by-shot fluctuations.

For the x-ray cavity alignment, five different types of XBPMs will be used:

(i) Coarse-alignment XBPMs with cerium-doped yttrium aluminum garnet (YAG:Ce) scintillators (X_{21}, X_{23}, X_{31}, and X_{41})[1] or boron-doped diamond (diamond:B) scintillators (X_{11} and X_{42}) are used to guide x-rays reflected from diamond crystals and build the rectangular orbit in the first approximation. Each XBPM is furnished with a 250-μm alignment hole in the scintillator. The alignment holes will be placed before the x-ray cavity alignment on the nominal x-ray rectangular trajectory.

(ii) Diamond microscopes (C-microscopes) M_1–M_4 that look at the diamond crystals C_1–C_4 will be used to monitor the x-ray beam position on each diamond crystal, so that the beam can be aimed precisely on the desired location inside the crystal working area. (The working area has previously been identified [24,29] by using various x-ray metrology techniques.)

(iii) A minimally invasive (x-ray transparent) XBPM (X_{24}) with a diamond:B scintillator (without a hole) is designed to provide fine alignment by monitoring and 2D overlapping the x-ray beams circulating over multiple round trips in the cavity and with the electron orbit. It is located in the midpoint of the round trip and is assumed to provide beam information equivalent to what would be measured at the effective source point (undulator center) [19].

(iv) Time-resolved XBPMs X_{10} and X_{40} use fast cerium-doped yttrium aluminum perovskite (YAP:Ce) scintillators to image x-ray beam profiles differentially in time with ns resolution. These components provide a complementary approach to achieving 2D spatial overlap between the x-ray beams and the electron orbit.

(v) XBPM X_{20} on the diffracted beam sample using a YAG:Ce scintillator is designed for monitoring the position and beam profile at the upstream end of the system, providing information on beam properties close to the condition when it re-enters the undulator.

The initial 45° angular orientation of crystal C_1 is determined by matching the energy of the photons in the 400 Bragg reflection from C_1 to the photon energy in the 440 Bragg back-reflection from diamond crystal C_x (in station G) [24]. The angles of diamond crystals C_2–C_4 are set into the position of the 400 Bragg peak reflectivity by minimizing the x-ray transmission intensity, which is monitored by the corresponding XBIMs D_2–D_4, running in time-averaged mode.

Si-based XBIMs D_1–D_4 and intracavity minimally invasive diamond-based XBIM D_d must work in time-resolved mode with ns resolution to measure the photon intensity of the individual x-ray pulses after each round trip. This is essential for accurate ($\lesssim 100$ nrad) angular alignment of the diamond crystals [19] and for measuring and maximizing the cavity ringdown. In the final step, the cavity round-trip time is adjusted to the time delay of the second electron bunch to achieve its 3D overlapping with the circulated x-ray pulse and thus to initiate lasing. Lasing is monitored and the CBXFEL gain is measured with XBIMs D_d, D_1, and D_5.

The CBXFEL pulses are expected to have an energy bandwidth ranging from a few meV in the XFELO mode to $\simeq 50$ meV in the XRAFEL mode. To measure such narrow x-ray pulse spectra, a meV-resolution single-shot spectrograph was designed based on the principles of angular-dispersive x-ray crystal optics [30]. The detailed design and characterization of this meV-resolution spectrograph will be discussed in a separate publication [31].

The diagnostic components have been designed based on the estimated photon flux of the undulator radiation for the CBXFEL project, as tabulated in Table II [32]. The alignment of all x-ray optical components will be performed in the XRAFEL mode because it provides more photons ($\simeq 3.6 \times 10^7$ ph/s/100 meV) than the XFELO mode. The diagnostic components are designed correspondingly to be sensitive to an average photon flux of $\sim 10^7$ ph/s—the flux of the monochromatic beam in the cavity.

The diagnostic components have been tested and characterized with pulsed x-ray beams at the Advanced Photon

---

[1] The XBPMs are numbered with a two-digit subscript, in which the first digit indicates the nearest diamond crystal mirror number and the second digit indicates the XBPM's place in sequence away from that crystal (e.g., X_{21} refers to the first XBPM near crystal C_2).

Source (APS) bending magnet beamline 1-BM and undulator beamlines 4-ID and 7-ID and at the LCLS. In the following sections, each type of diagnostics will be discussed in detail.

III. X-RAY BEAM POSITION/PROFILE MONITORS

X-ray beam position and profile monitors define and monitor the x-ray beam transverse (x, y) trajectory and profile in the CBXFEL cavity. They must be minimally invasive and retractable from the x-ray beam path when not in use. The XBPMs used in this project are scintillator-based imaging x-ray detectors with μm resolution. Such detectors were introduced in 1990s and have been in use since then at synchrotron and XFEL facilities [33–36]. They are composed of a partially transparent scintillator screen, an optical imaging system, and a digital camera.

A. Luminescent XBPMs for coarse alignment

XBPMs of this type are designed to work under low flux conditions (10^5–10^7 ph/s) with a spatial resolution of less than 10 μm. Most of the coarse-alignment XBPMs in this project use YAG:Ce scintillators with high sensitivity and light yield [36]. They have a sensitive area of $\sim 14 \times 10$ mm^2 and a thickness of 100 μm.

The diamond:B scintillator (10×10 mm^2 and 30-μm thick) with lower sensitivity to x-rays is used in X_{11} as x-ray imager to prevent saturation due to the intense, direct x-ray undulator beam. The same type of scintillator is also used in X_{42} as both x-ray or electron beam imager.

Each coarse-alignment XBPM uses a low-noise Prosilica GT5400 camera with a large field of view (18.8×10.6 mm^2, pixel size 3.45 μm) and a long-working-distance (≃183 mm) microscope (Infinity KC VideoMax with IF-3 objective lens) as the 1∶1 imaging camera and optic.

Figure 2(a) shows a schematic of the setup for the coarse-alignment YAG:Ce XBPM. The scintillator is mounted at 45° to the x-ray beam, while the optic and camera are mounted looking at 90° to the scintillator. An alignment hole is laser machined in the scintillator (by PALM Scientific) such that the x-ray beam passes a circular hole having 250 μm diameter through the entire scintillator thickness. Elliptical markings with an aspect ratio of $1:\sqrt{2}$ (repeating every 0.5 mm along the minor axis) are machined on the scintillator to help track the beam position, as shown in the inset in Fig. 2(a).

Figure 2(b) shows an image of a 1×1-mm^2 x-ray beam captured by the XBPM illuminated with 3×10^9 9.831-keV photons.[2] The elliptical markings on the scintillator can be clearly seen from this measurement. Figure 2(c) shows an image of a 0.1×0.1-mm^2 x-ray beam with $\sim 10^7$ photons, corresponding to the worst-case scenario in the CBXFEL experiment. The signal-to-noise ratio (SNR) under this condition is around 11.

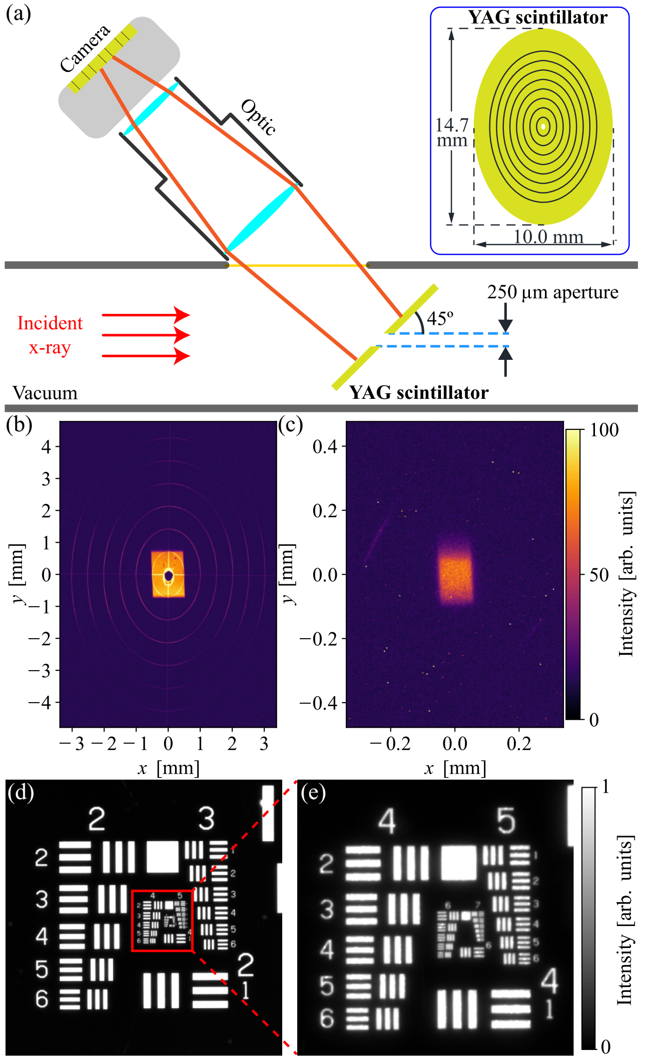

FIG. 2. Schematic and performance of the coarse-alignment YAG:Ce XBPM. (a) Schematic of the coarse-alignment XBPM with a 100-μm-thick YAG:Ce scintillator. (b) Image of a 1×1 mm^2 x-ray beam with 3×10^9 9.831-keV photons. (c) Similar to (b) but with a 0.1×0.1 mm^2 (FWHM) beam with $\sim 10^7$ photons. (d) Image of a standard 1951 USAF resolution test target taken by the optic and camera at the designed working distance. (e) Zoom-in view of the central part of (d).

Using a standard 1951 USAF resolution test target, the combined resolution of the optic and the camera was tested at the design value for the working distance (183 mm) with 1∶1 magnification. As shown in Figs. 2(d)–(e), the XBPM has a resolution of ∼6 μm because it resolves the fourth element in group 6 in the USAF target, which has a line width of 5.52 μm.

---

[2] The absolute photon flux is measured using a Si photodiode with a large active area calibrated at Physikalisch-Technische Bundesanstalt [37].

1. $\boldsymbol{X_{11}}$ *and* $\boldsymbol{X_{42}}$ *with diamond:B scintillators*

Because X_{11} sees the direct intense undulator beam, a 30-μm-thick diamond:B scintillator is used in this XBPM to avoid saturation. The same scintillator type is used in X_{42}; however, at that position, the XBPM is first used to detect the direct electron beam (with the chicane powered down) and thus to determine the location of the undulator axis; then it is used to detect x-rays reflected from C_4 (see Appendix for details). As with the YAG:Ce scintillators, the diamond:B scintillator is machined with an alignment hole but without any elliptical markings. The same diamond:B scintillator type is also used in X_{24}. X-ray tests of this type of scintillator are presented in Sec. III C.

2. In-air YAG:Ce $\boldsymbol{X_{13}}$

For all XBPMs except X_{13}, the scintillator is mounted in a vacuum tank; X_{13} is mounted in air in station G, which is located about 250 m downstream of the undulator. We note that X_{14} is actually the same as X_{13}, just moved to another location downstream of the channel-cut crystal monochromator CC (see Fig. 1). The x-ray beam size expands to ∼0.7 mm after propagation of 250 m and has a significantly reduced photon density. Therefore, an optical system with better noise reduction and photon collection is needed. The camera and optic used in X_{13}/X_{14} are the same as those used in X_{24} and are discussed in detail in Sec. III C.

B. Diamond microscopes $\mathbf{M_1}$–$\mathbf{M_4}$

Diamond microscopes M_1–M_4 are designed to monitor the x-ray beam on diamond crystals C_1–C_4, respectively, and to adjust the crystal position such that the x-ray beam is aimed and reflected from particular locations on the crystal's working area. The working areas of C_1–C_4 were identified previously [23] using x-ray metrology techniques. These microscopes are designed similar to the coarse-alignment XBPMs with one exception: the diamond crystal itself serves as the scintillator, producing significant fluorescence due to impurities when exposed to x-rays [38,39]. The resolution of the microscope is required and designed to be less than 10 μm (similar to the coarse-alignment XBPMs).

A schematic of the setup for x-ray tests of the C-microscope is shown in Fig. 3(a). The diamond crystal mirror is mounted perpendicular to the x-ray beam. Figure 3(b) shows the fluorescence map recorded by the microscope when one of the diamond crystal mirrors is exposed to a $4.2 \times 2.5\ \mathrm{mm}^2$ x-ray beam. The diamond crystal fluorescence strength is not homogeneous. The regions with fewer impurities [$0.2\ \mathrm{mm} < x < 2.2\ \mathrm{mm}$, $1.5\ \mathrm{mm} < y < 2.5\ \mathrm{mm}$, i.e., growth sector (001)] that produce less fluorescence [38,39], and regions with more impurities can be distinguished. Figure 3(c) shows a clear, bright, rectangular spot with $\mathrm{SNR} = 18$ recorded when the diamond crystal is illuminated with an x-ray beam with parameters close to the CBXFEL conditions: $\simeq 100 \times 60\ \mu\mathrm{m}^2$ footprint and $\sim 10^7$ photons.

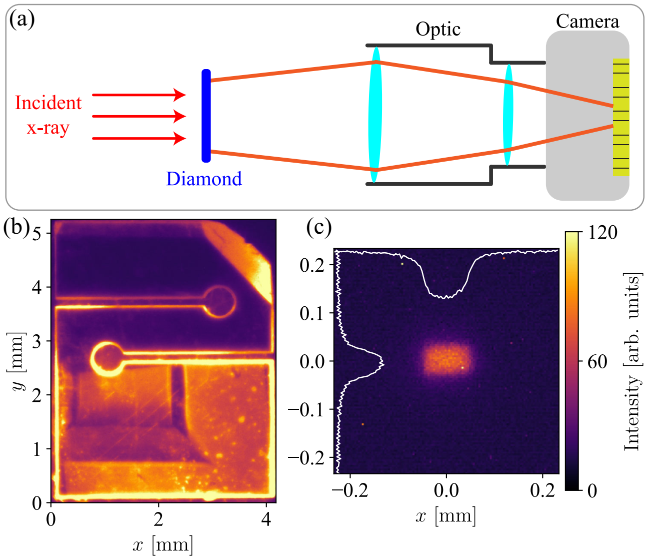

FIG. 3. Scintillation test of the diamond Bragg-reflecting crystal mirrors. (a) Schematic of the scintillation test with x-rays. (b) An x-ray beam with $\sim 10^9$ photons and a footprint of $4.2 \times 2.5\ \mathrm{mm}^2$ illuminates the entire bottom part of the diamond crystal. (c) An x-ray beam with $\sim 10^7$ photons and a $\simeq 100 \times 60\ \mu\mathrm{m}^2$ footprint (close to the CBXFEL conditions) illuminates a smaller region around the center of the crystal working area. The white curves are the projections of the beam image onto horizontal and vertical directions.

C. Minimally invasive luminescent $\mathbf{X_{24}}$

Although the beam size and position in the effective x-ray source point (in the middle of the undulator) are not easy to measure directly, they can be measured indirectly at the symmetric point located at the midpoint between crystals C_2 and C_3. A minimally invasive XBPM placed at this location can measure the x-ray beam position over multiple passes in the cavity while having minimal effect on the beam. The multipass measurement permits correction of the spatial offset in the x-ray orbit caused by positional misalignment of the crystals and achieves 2D spatial overlap between the x-ray beams and the electron orbit (see Ref. [19] and Appendix for details).

For this purpose, X_{24} is designed with a 30-μm-thick diamond:B scintillator with a transparency of 97% for 9.831-keV x-rays. Such diamond:B scintillators produce 15 ± 5 times weaker signals than the 100-μm YAG:Ce scintillators. Therefore, this XBPM requires an optic with a larger numerical aperture and a camera with lower noise, compared to the coarse-alignment XBPMs. For X_{24}, we use an Infinity K2 DistaMax long-distance microscope with objective lens CF-3 and an Andor Zyla 4.2 Plus camera (field of view: $13.3 \times 13.3\ \mathrm{mm}^2$, pixel size 6.5 μm).[3]

---

[3] The same optic and camera are also used in the in-air XBPM X_{13}/X_{14} to detect weak x-ray signals outcoupled from the cavity.

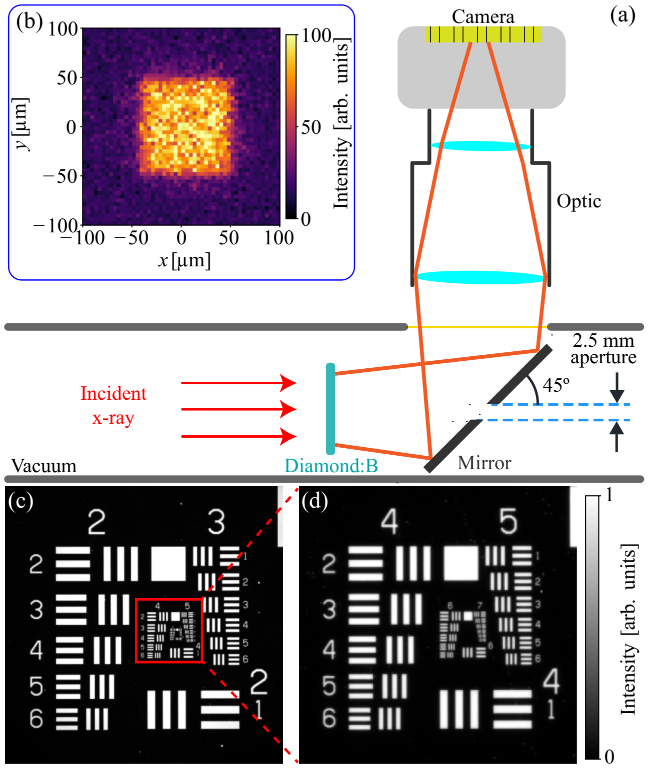

FIG. 4. Schematic and performance of the minimally invasive XBPM X_{24}. Note that part (b) has been positioned at the upper left for the economy of presentation. (a) Schematic of setup for x-ray tests of X_{24}. (b) An image captured by X_{24} when the diamond scintillator is illuminated with a 0.1 × 0.1 mm^2 (FWHM) x-ray beam with $\sim 10^7$ of 9.831 keV photons. (c) Image of a standard 1951 USAF resolution test target placed in the location of the diamond:B scintillator. (d) Zoom-in view of the central part of (c).

The schematic of the setup of X_{24} is shown in Fig. 4(a). The diamond:B scintillator is mounted perpendicular to the x-ray beam. The fluorescent photons are reflected to the optic and the camera from a flat mirror placed downstream of the scintillator at 45°. The mirror has a custom-made hole of ∼2.5 mm in diameter to transmit x-rays circulating in the cavity. Figure 4(b) shows an image of a 0.1 × 0.1 mm^2 x-ray beam with $\sim 10^7$ 9.831-keV photons. The SNR of this XBPM is around 21, which is about twice as large as the SNR of the coarse-alignment XBPMs.

The spatial resolution of the optical system is measured at the design working distance of 95 mm using the standard 1951 USAF target, as shown in Figs. 4(c) and 4(d). This optical system can also resolve the fourth element in group 6 of the target, which has a line width of 5.52 μm, indicating that this system has a spatial resolution of ∼6 μm, the same as the coarse-alignment XBPMs.

D. Time-resolved XBPMs X_{10}, X_{40}

One way to establish the 2D spatial overlap between the returned x-ray pulse and the electron bunch is to directly visualize the position of the returned x-ray beam trajectory with respect to the nominal trajectory of the electron beam. For this purpose, station F and station A each host a time-resolved XBPM with YAP:Ce screens. At the upstream end, the electron beam will be visualized by observing the luminescence from a thin diamond:B screen (X_{42}), while the returned, and thus delayed, x-ray beam is visualized via x-ray induced luminescence from a thin YAP:Ce screen (<30 μm) in X_{10} in station A. The downstream monitor, X_{10}, allows comparison of the x-ray beam position before and after the x-ray beam has completed the first round trip. It is positioned after reflection at mirror C_1, where radiation background from the SASE full bandwidth and the chicane bend is significantly lower.

Both of these time-resolved XBPMs use an Andor iStar scientific sCMOS camera. The Andor iStar camera has the capability for electronic gating via an integrated multiple-channel plate intensifier. It allows the capture of both ultraviolet and optical wavelengths. Ultraviolet imaging optics are used to image the x-ray beam profile at a time window delayed by the duration of one cavity round trip, taking advantage of a short fluorescence lifetime of YAP:Ce (∼25 ns at 370 nm). The combined time resolution of the imaging system is ∼32 ns. The image quality can be improved by using a multipulse long exposure with synchronized a short electronic gating, as previously demonstrated [40].

E. Intracavity beam profile monitor X_{20}

To monitor the circulating x-ray pulse intensity within the x-ray cavity, one approach is to use a diamond transmission grating to pick up a *beam sample* [27]. The angularly separated beams, in the form of the ± diffraction orders, can be spatially separated after propagating over a large distance and directly measured with either a diode D_5 or a scintillator screen X_{20}. This scheme is implemented in the cavity diagnostic system by having a grating available to be inserted and retracted in station C, and a beam profile and a beam intensity monitor in station E. When the transmission diamond grating Gr is inserted in station C as shown in Fig. 1, the x-ray beam diffracts into multiple branches. The center branch contains the majority of x-ray power and continues to circulate in the cavity. The diffracted ±1 order, as the primary beam sample, is captured by XBIM diode D_5 and XBPM X_{20}. The transmission grating has a period of 1 μm, which introduces ∼4 mm separation between the zeroth and first diffraction orders at the C_3 crystal, allowing the two beam samples to bypass C_3 and reach station E. For the high-gain XRAFEL configuration, we anticipate using a grating with a higher first order efficiency of ∼5% and zeroth order transmission greater than 80%. For the low-gain XFELO configuration, a lower-loss grating will be used, with the first order efficiency of ∼1% and zeroth order transmission greater than 95%. From the sampled first order beam, XBIM D_5

TABLE III. Summary of the different types of XBPMs designed, manufactured, and tested for the CBXFEL project. All x-ray tests were performed at the APS 1-BM beamline [41].

XBPM	X_{11}, X_{42}	X_{21}, X_{23}, X_{31}, X_{41}	X_{24}	X_{13}/X_{14}	M_1–M_4
Scintillator	Diamond:B 30-μm thick with reference hole	YAG:Ce 100-μm thick with reference hole	Diamond:B 30-μm thick	YAG:Ce 100-μm thick	Diamond crystal mirrors (C_1–C_4)
Geometry[a]	45°	45°	90°	90°	45°
Optic	VideoMax[b] NA = 0.06 MAG = 1.0	VideoMax NA = 0.06 MAG = 1.0	DistaMax[b] NA = 0.19 MAG = 1.8	DistaMax NA = 0.19 MAG = 1.8	VideoMax NA = 0.06 MAG = 1.0
Camera	Prosilica GT-5400[c]	Prosilica GT-5400	Andor Zyla 4.2 Plus[d]	Andor Zyla 4.2 Plus	Prosilica GT-5400

[a] Angle between the scintillator and incident x-ray beam.
[b] From Infinity Photo-Optical Company. NA, numerical aperture and MAG, magnification.
[c] Pixel size is 3.45 μm. Field of view is 18.8×10.6 mm^2. Dark noise is 2.3 e$^-$.
[d] Pixel size is 6.5 μm. Field of view is 13.3×13.3 mm^2. Read noise is less than 1 e$^-$.

measures the circulating pulse train, as described in the next section, and XBPM X_{20} (with a YAG:Ce screen) captures the beam position and profile. This XBPM enables constant monitoring of the beam position at a location near the undulator entrance. This is particularly useful for monitoring angular errors of C_1 and C_2 when they are translated simultaneously for cavity round-trip length adjustment.

F. Summary of XBPMs

Tables III and IV summarize the characteristics and the performance of all types of XBPM developed for this project. The combined use of all these XBPMs during different alignment stages is critical to achieve the desired sub-μrad angular and μm spatial alignment accuracy, to maximize the cavity quality factor, and to optimize the two-pass CBXFEL gain.

All XBPMs were designed to meet the CBXFEL project physical requirements and tested with APS x-ray beams in air. In the CBXFEL experiment, most of the XBPM scintillators (except for X_{13}) will be integrated into the ultra-high-vacuum (UHV) environment and will be controlled remotely.

TABLE IV. Continuation of Table III presenting XBPMs designed, manufactured, and tested for the CBXFEL project at LCLS.

XBPM	X_{10}, X_{40}	X_{20}
Scintillator	YAP:Ce 30-μm thick	YAG:Ce 200-μm thick
Geometry	80°	90°
Optic	Thorlabs NA = 0.16 MAG = 2.0	Navitar NA = 0.07 MAG = 2.0
Camera	Andor iStar sCMOS	Andor Zyla 4.2 Plus

IV. X-RAY BEAM INTENSITY MONITORS

During CBXFEL alignment, the XBIMs must be operated both in time-averaged mode and in time-resolved mode with nanosecond resolution. The present diagnostic system uses two types of XBIMs: silicon-based and diamond-based. The ns-resolution silicon-based XBIMs are operated in two contexts: D_1–D_4 operate in air and D_5 operates in vacuum. The diamond-based detector D_d, which is UHV-compatible, provides minimally invasive monitoring of x-ray beam intensity inside the UHV cavity with ns resolution. A large dynamic range of $\gtrsim 10^5$ is required for all XBIMs to achieve the highest sensitivity to crystal misalignment and to measure and maximize cavity ringdown.

The XBIMs were tested with 9.831-keV x-ray photon pulses of $\simeq$50-ps duration incident at a repetition rate of 6.5 MHz. APS beamlines 1-BM [41] and 7-ID [42] were used for measurements with low and high photon flux values, respectively.

A. ns-Resolution Si XBIMs D_1–D_4 and D_5

X-ray beam intensity monitors D_1–D_4 and D_5 are critical both for the initial and final alignment of the cavity and for measuring cavity ringdown and CBXFEL gain. The in-air XBIMs D_1–D_4 measure x-rays transmitted through diamond crystal mirrors C_1–C_4, respectively. Low transmissivity indicates high reflectivity at the Bragg reflection peak, while high transmissivity signals that the crystal angle is off the reflection peak position. Thus, XBIMs D_1–D_4 serve as very sensitive angular encoders of crystal mirrors C_1–C_4, respectively.

For this project, Si photodiodes (Thorlabs SM05PD1A) are used as XBIMs D_1–D_4. DC power supplies are used to provide 20-V bias voltage via bias tee (Thorlabs PBM42). The photodiode signal is digitized using a 14-bit low-noise ($\lesssim$0.1 mV) digitizer (Teledyne ADQ14) with a 500-MHz

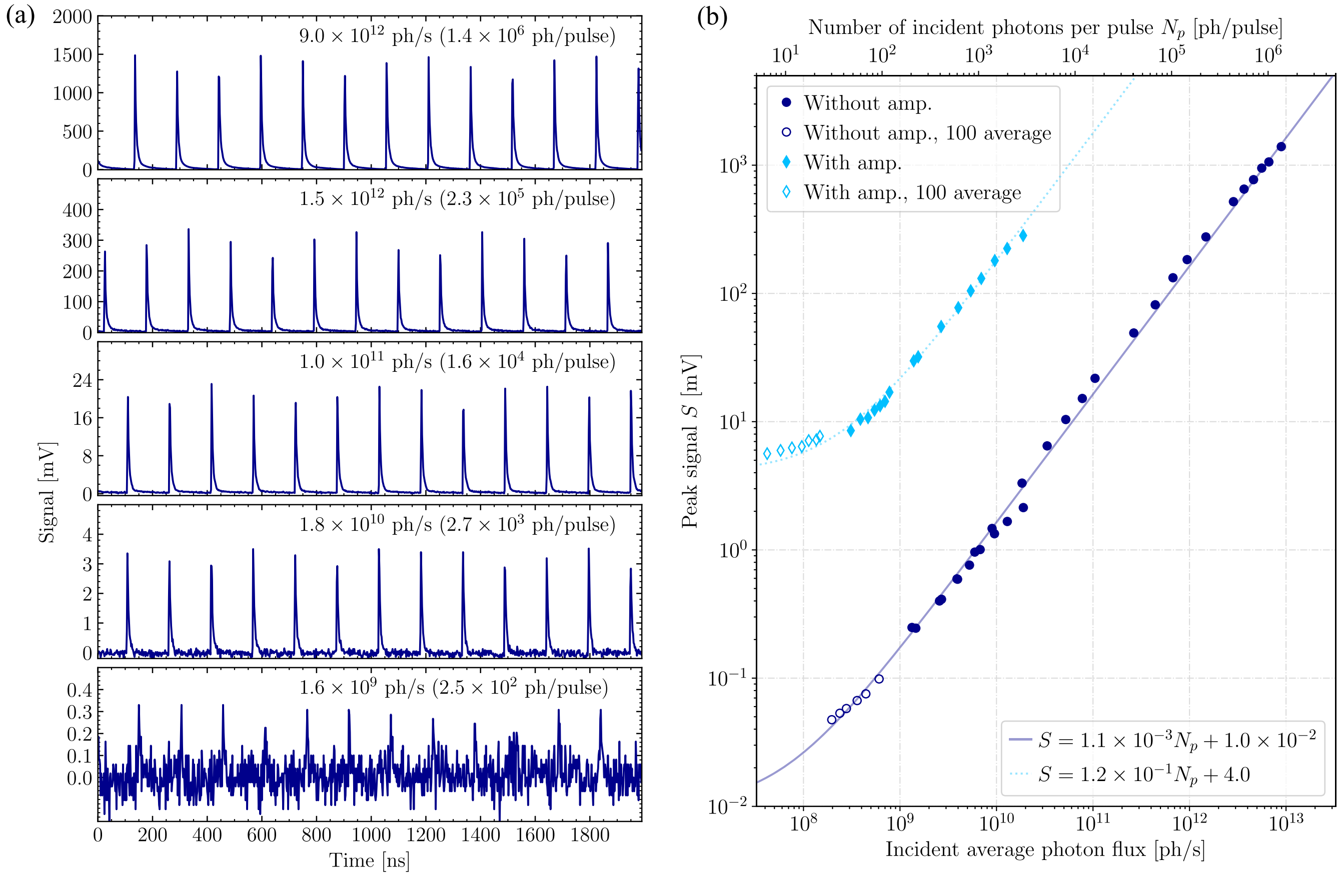

FIG. 5. Test results of Si XBIM (Thorlabs SM05PD1A) with 9.831-keV x-ray photon pulses. (a) Si XBIM signals (without amplifier) measured at different incident x-ray photon flux values. (b) Calibration curves of the Si XBIM without (dark blue circles) and with amplifier (light blue diamonds) as a function of the incident photon flux (or number of photons per pulse N_p). Open markers show the data averaged over 100 pulses. The lines present the linear fit to the experimental data with fit parameters given in the bottom-right box.

sampling rate and EPICS control. A UHV-compatible Si photodiode (Opto Diode AXUV20HS1) is used for XBIM D_5.

Figure 5(a) shows examples of Si-based XBIM signals measured at different values of incident average photon flux or, alternatively, photons per pulse. The Si XBIMs have a ns response with a ∼4-ns rise time. The detector peak signal values measured at different incident average photon flux (or alternatively at different number of photons per pulse) are shown as solid dark blue circles in Fig. 5(b). The data can be fitted well with a linear calibration curve presented by the solid dark blue line. Apparently, such XBIMs can detect photon pulses with intensities in a broad range from the minimum detectable number of photons per pulse (MDP) of ∼200 ph/pulse to $\sim 2\times 10^6$ ph/pulse. Here, the upper end of the range is limited by the digitizer maximum input signal of 2 V. The MDP is limited by the digitizer noise ($\lesssim 0.1$ mV) but can be improved by averaging over multiple pulses. The open dark blue circles in Fig. 5(b) show the measured mean pulse peak values after averaging over 100 pulses. Obviously, the MDP has been improved significantly—from ≃200 to ≃30 ph/pulse—by the averaging procedure.

Alternatively, the MDP can be improved by using an amplifier. With a high-speed 2-GHz bandwidth amplifier (Femto HSA-X-2-40), the MDP is ≃40 ph/pulse without averaging, as shown by the solid light blue diamonds in Fig. 5(b). With averaging over 100 pulses, the MDP drops to $\lesssim 10$ ph/pulse, as shown by the open light blue diamonds in Fig. 5(b). The solid light blue line is a linear fit—the calibration curve—to the experimental data.

While the amplifier helps with reaching smaller MDP values, the amplified signal saturates the digitizer already at $\simeq 1.7\times 10^4$ ph/pulse. Therefore, to measure in a broader pulse intensity range, switching between nonamplified to amplified modes is required. We use a coaxial switch (Radiall R570463100) that takes the output signal from the XBIM as input and has two output channels: one to the amplifier and one directly to the digitizer. Only one of the two channels can be remotely selected for connection at a time. This switch enables the combined use of the XBIM with and without the amplifier, allowing the XBIM to cover

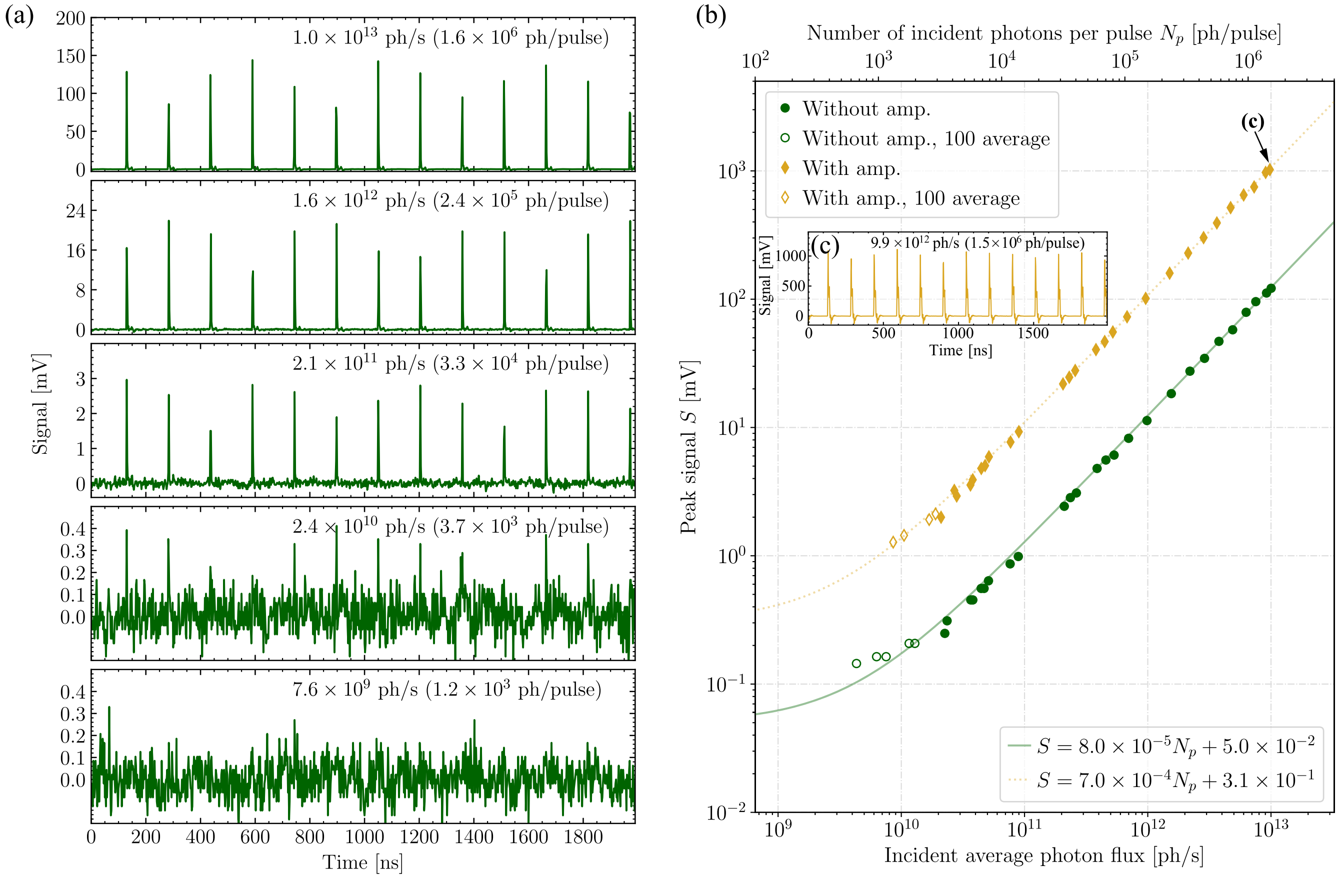

FIG. 6. Similar to Fig. 5, but for diamond-based XBIM D_d (Sydor Technologies M102). The inset (c) shows the D_d signal measured with an amplifier, corresponding to the position indicated by the arrow on the upper calibration curve in (b).

a large dynamic range of incident photon pulse intensities from 10 ph/pulse to 2×10^{6} ph/pulse.

B. ns-Resolution diamond XBIM $\mathbf{D_d}$

The x-ray cavity ringdown and CBXFEL gain can be measured directly by the intracavity XBIM D_d (see Fig. 1) without outcoupling of the x-ray pulses circulating inside the cavity, provided D_d is a minimally invasive (x-ray transparent) beam intensity monitor with ns time resolution. Such devices became available due to the recent development of diamond-based x-ray detectors for pulsed x-rays [43,44]. An x-ray–transparent XBIM with a 45-μm-thick diamond x-ray sensor that is 96.5% transparent to 9.8-keV x-rays was acquired from Sydor Technologies (UHV-compatible model M105UHV-T) and characterized with x-ray pulses for this purpose. After several iterations of x-ray tests (with the x-ray pulse parameters close to the CBXFEL case) and subsequent detector modifications by the vendor, the performance of this device was optimized to produce clean signals with fast time response.

Figure 6(a) shows examples of signals measured by such a diamond-based XBIM in response to incident photon pulses of different intensities. The detector is biased with 20 V via a coaxial cable. Another coaxial cable is used to read the signal with a digitizer (Teledyne ADQ14). Although the diamond XBIM is sensitive to x-ray pulses over a large intensity range, there are significant pulse-to-pulse peak height fluctuations because the response time of the XBIM is shorter than the 2-ns time resolution of the digitizer.

The detector pulse peak values as a function of the photon pulse intensity, or alternatively as a function of the average photon flux values, are shown in Fig. 6(b) with dark green solid circles. The diamond XBIM can detect photon pulses over a wide range of intensities from MDP = 3×10^{3} ph/pulse to at least 10^{7} ph/pulse. Here the maximum number is an estimate limited only by the available intensity of x-ray photon pulses from the undulator source. By averaging over 100 pulses, the MDP improves to ≃700 ph/pulse (see data points presented by open dark green circles). The experimental data can be fitted well with a linear calibration curve, presented by the solid line.

To reduce the pulse-to-pulse fluctuation, a variable-gain current amplifier (Femto DHPCA-100) with a low-pass filter was used. The optimal pulse shape was achieved with the amplifier set to the low-noise mode with a transimpedance gain of 10^{3} and an 80 MHz bandwidth.

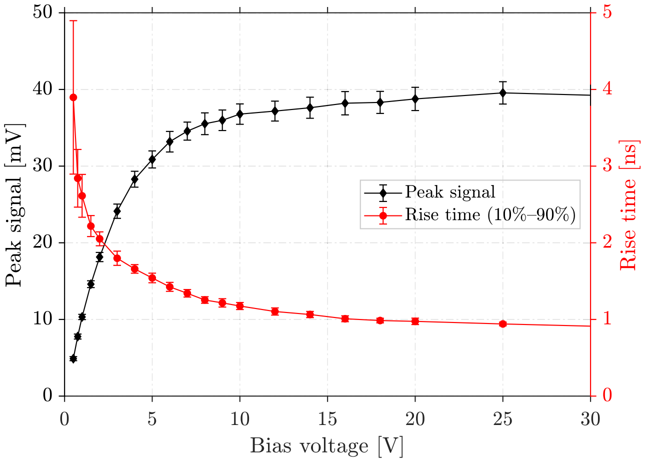

FIG. 7. Pulse peak value and pulse rise time of the diamond-based XBIM (Sydor M102) measured as a function of the bias voltage with a fast oscilloscope.

This approach greatly reduced the high-frequency noise and pulse-to-pulse fluctuation of the signal, as shown in Fig. 6(c). The calibration curve of the diamond XBIM measured under these conditions is presented by solid gold diamond markers, which are fitted well with a linear graph in Fig. 6(b). Using the amplifier does not significantly improve the MDP value but does limit the maximum detectable photon pulse intensity because the amplifier output signal becomes saturated. Averaging over 100 pulses reduces MDP to $\simeq 10^3$ ph/pulse. As with the D_1–D_4 Si-based XBIMs, the diamond-based XBIM D_d can be connected to a coaxial switch to measure sequentially with or without the amplifier.

To better characterize the time characteristics of the diamond-based XBIM, a fast oscilloscope (Keysight MSO9404A) with a 4-GHz bandwidth and a sample rate of 20 GSa/s (i.e., 50-ps time resolution) was used to digitize the nonamplified XBIM signal. Figure 7 shows the peak pulse value and pulse rise time (at a 10%–90% level) measured as a function of bias voltages under conditions of a constant incident photon pulse intensity of 8×10^5 ph/pulse. Obviously, the pulse peak level saturates when the bias voltage reaches $\simeq$15–20 V. Simultaneously, the rise time shortens to $\lesssim 1$ ns. This result shows that 20 V is an optimal bias voltage for this device.

Altogether the studies presented in this section show that the Sydor M102 diamond-based XBIM is an appropriate device to be used as the minimally invasive time-resolved XBIM D_d in the CBXFEL experiment.

V. SUMMARY

In summary, an x-ray diagnostic system and its components were developed for precise alignment of the x-ray optical elements of the CBXFEL x-ray cavity (with sub-μrad angular and μm spatial accuracy) and for achieving three-dimensional overlapping of the electron and photon beams in the cavity. The R&D was performed within the framework of a joint CBXFEL collaborative project involving Argonne National Laboratory, SLAC National Accelerator Laboratory, and Spring-8 [20].

Three types of diagnostic components were designed: x-ray beam position and profile monitors (XBPMs), x-ray beam intensity monitors (XBIMs), and a meV-resolution x-ray spectrograph. The XBPM and XBIM components, reported in this paper, were designed, prototyped, and characterized at the Advanced Photon Source.

Four types of XBPMs were designed and characterized with x-rays to demonstrate their ability to monitor x-ray beam position and profiles in the cavity with a resolution better than 10 μm, assuming photon pulses of a relatively small intensity of 10^7 ph/pulse. The four types are (i) coarse-alignment luminescent XBPMs using YAG:Ce or diamond:B scintillators furnished with x-ray alignment holes; (ii) diamond microscopes to monitor the beam position on the diamond crystal mirrors; (iii) a minimally invasive diamond luminescent XBPM that is 97% transparent to x-rays for fine alignment; and (iv) time-resolved XBPMs with YAP:Ce scintillators to provide the ability to directly measure beam positions after each round trip at both the up- and downstream ends of the cavity.

Two types of XBIMs with ns time resolution were developed as required for sub-μrad angular alignment of the x-ray crystal mirrors as well as for measurement of x-ray betatron oscillations [19], cavity ringdown, and CBXFEL gain.

The Si-based XBIMs D_1–D_5, each coupled to a low-noise digitizer, are sensitive to x-ray pulse intensities in a broad range from $\simeq 40$ to $\simeq 2 \times 10^6$ ph/pulse; the full range is accessed by operating both with and without an amplifier. By averaging signals over 100 pulses, the minimal detectable number of photons per pulse (MDP) can be reduced to 10 ph/pulse, which is essential for a finer cavity alignment and for better detection of the x-ray betatron oscillations.

The intracavity minimally invasive (96.5% transparent) diamond-based XBIM D_d has a sharp time response, with a rise time of less than 1 ns. It is capable of measuring the intracavity pulse intensity in the range 3×10^3 ph/pulse to at least 10^7 ph/pulse. When the signal is averaged over 100 pulses, the MDP value drops to 700 ph/pulse. Si diode D_5, together with a transmission diamond grating, provides similar sensitivity to the recirculating pulse intensity, measuring a 1%–5% beam sample.

A meV-resolution single-shot spectrograph was designed to measure narrow-band energy spectra of the CBXFEL x-ray pulses. A preliminary test of the spectrograph at the APS 1-BM beamline showed an energy resolution of ~15 meV. The detailed design and characterization of the spectrograph will be discussed in a separate publication [31].

ACKNOWLEDGMENTS

Kwang-Je Kim, Marion White, Ryan Lindberg, Lahsen Assoufid (ANL), Zhirong Huang, and Gabriel Marcus (SLAC) are acknowledged for discussions and support. We are grateful to Michael Wojcik, Alan Kastengren, Troy Lutes, Jeff Hoffman, Mark Engbretson, Keshab Kauchha, and Daniel Haskel (ANL) for support with experiments at APS beamlines 1-BM, 4-ID, and 7-ID. Peter. J. Heesterman (United Kingdom Atomic Energy Authority) is acknowledged for providing the EPICS driver for the Teledyne ADQ14 digitizer. Yuri Shvyd'ko is indebted to Andreas Koch and Wolfgang Freund (European XFEL) for extensive discussions of the x-ray beam imagers as well as to Jen Bohon and John Smedley (LANL) for detailed information on the time-resolved diamond-based x-ray sensors. This research used resources of the Advanced Photon Source, a U.S. Department of Energy (DOE) Office of Science user facility at Argonne National Laboratory and is based on research supported by the U.S. DOE Office of Science-Basic Energy Sciences, under Contract No. DE-AC02-06CH11357. Work at SLAC is supported by the U.S. Department of Energy, Office of Science, Office of Basic Energy Sciences under Contract No. DE-AC02-76SF00515.

APPENDIX: CBXFEL ALIGNMENT PROCEDURE

A.1 *No-beam prealignment.*

A.1.1 All XBPMs, diamond crystals C_1–C_4, and lenses L_1–L_2 are prealigned in all stations (before installation in the undulator tunnel) to design positions with a spatial precision of $\simeq 10$ μm and angular accuracy of $\simeq 2$ mrad.

A.1.2 All stations are installed on girders in the undulator tunnel and properly aligned.

A.2 *Prealignment with e-beams and x-ray beams.*

A.2.1 A single-bunch e-beam is on. Chicanes are off. Chicanes are designed and tested to produce negligible disturbance to the nominal undulator axis.

A.2.2 The e-beam position in station B is determined by using X_{42} to a precision of <10 μm. The X_{42} reference hole center is moved to the location of the e-beam center. All optical and diagnostic elements in station B are moved appropriately by the same amount.

A.2.3 The chicanes are on and thermalized.

A.2.4 The x-ray beam is on. The undulator x-ray beam position in station A is determined by using X_{11} to a precision of <10 μm. The X_{11} reference hole center is moved to this location. All elements in station A are moved appropriately by the same amount.

A.3 *Single-bunch x-ray alignment.*

A.3.1 The e-beam is optimized for the highest x-ray spectral flux at the designed photon energy.

A.3.2 X-rays are reflected from diamond crystals C_1–C_4 and are guided through the reference holes of the coarse alignment XBPMs with a $\simeq$10-μm spatial and a few μrad accuracy. Bragg back-reflection diamond crystal C_x is used for initial C_1 angular alignment [24]. Lenses L_1–L_2 are bypassed.

A.3.3 The fine angular alignment of crystals C_1–C_4 with a $\lesssim 100$ nrad accuracy is achieved by monitoring with XBIMs D_1–D_5 and D_d of the x-ray beam circulating in the cavity, maximizing the lifetime of the x-ray beam ringdown (RD), and minimizing the amplitude of the x-ray beam betatron oscillations (BO) [19].

A.3.4 The 2D overlap of the x-ray beam with the e-beam is achieved by translating one of the diamond crystals (C_2 or C_4) and monitoring the overlap of the multipass x-ray beams on X_{24}, X_{40}, and X_{10}.

A.3.5 Lenses L_1–L_2 are moved into the x-ray beam and their positions are optimized by maximizing RD and minimizing BO using XBIMs D_1–D_5, and D_d [19].

A.4 *Double-bunch x-ray alignment.*

The double-bunch e-beam is on. The longitudinal overlap of the e-beam with the x-ray beam (missing yet for the final 3D-overlap) is achieved by varying the double-bunch time separation or/and by adjusting cavity round-trip length and maximizing the XFEL gain using XBIMs D_1, D_5, and D_d.

---

[1] P. Emma, R. Akre, J. Arthur, R. Bionta, C. Bostedt, J. Bozek, A. Brachmann, P. Bucksbaum, R. Coffee, F.-J. Decker *et al.*, First lasing and operation of an ångstrom-wavelength free-electron laser, Nat. Photonics **4**, 641 (2010).

[2] J. Amann, W. Berg, V. Blank, F.-J. Decker, Y. Ding, P. Emma, Y. Feng, J. Frisch, D. Fritz, J. Hastings *et al.*, Demonstration of self-seeding in a hard-X-ray free-electron laser, Nat. Photonics **6**, 693 (2012).

[3] T. Ishikawa, H. Aoyagi, T. Asaka, Y. Asano, N. Azumi, T. Bizen, H. Ego, K. Fukami, T. Fukui, Y. Furukawa *et al.*, A compact X-ray free-electron laser emitting in the sub-ångström region, Nat. Photonics **6**, 540 (2012).

[4] W. Decking, S. Abeghyan, P. Abramian, A. Abramsky, A. Aguirre, C. Albrecht, P. Alou, M. Altarelli, P. Altmann, K. Amyan *et al.*, A MHz-repetition-rate hard X-ray free-electron laser driven by a superconducting linear accelerator, Nat. Photonics **14**, 391 (2020).

[5] C. Bostedt, J. D. Bozek, P. H. Bucksbaum, R. N. Coffee, J. B. Hastings, Z. Huang, R. W. Lee, S. Schorb, J. N. Corlett, P. Denes *et al.*, Ultra-fast and ultra-intense x-ray sciences: First results from the Linac Coherent Light Source free-electron laser, J. Phys. B **46**, 164003 (2013).

[6] C. Callegari, A. N. Grum-Grzhimailo, K. L Ishikawa, K. C Prince, G. Sansone, and K. Ueda, Atomic, molecular and optical physics applications of longitudinally coherent and narrow bandwidth free-electron lasers, Phys. Rep. **904**, 1 (2021).

[7] Y. Shvyd'ko, R. Röhlsberger, O. Kocharovskaya, J. Evers, G. A. Geloni, P. Liu, D. Shu, A. Miceli, B. Stone, W. Hippler *et al.*, Resonant x-ray excitation of the nuclear clock isomer ^{45}Sc, Nature (London) **622**, 471 (2023).

[8] J. Feldhaus, E. L. Saldin, J. R. Schneider, E. A. Schneidmiller, and M. V. Yurkov, Possible application of X-ray optical elements for reducing the spectral bandwidth of an X-ray SASE FEL, Opt. Commun. **140**, 341 (1997).

[9] E. L. Saldin, E. A. Schneidmiller, Y. V. Shvyd'ko, and M. V. Yurkov, X-ray FEL with a meV bandwidth, Nucl. Instrum. Methods Phys. Res., Sect. A **475**, 357 (2001).

[10] D. Ratner, R. Abela, J. Amann, C. Behrens, D. Bohler, G. Bouchard, C. Bostedt, M. Boyes, K. Chow, D. Cocco *et al.*, Experimental demonstration of a soft x-ray self-seeded free-electron laser, Phys. Rev. Lett. **114**, 054801 (2015).

[11] I. Inoue, T. Osaka, T. Hara, T. Tanaka, T. Inagaki, T. Fukui, S. Goto, Y. Inubushi, H. Kimura, R. Kinjo *et al.*, Generation of narrow-band X-ray free-electron laser via reflection self-seeding, Nat. Photonics **13**, 319 (2019).

[12] I. Nam, C.-K. Min, B. Oh, G. Kim, D. Na, Y. J. Suh, H. Yang, M. H. Cho, C. Kim, M.-J. Kim *et al.*, High-brightness self-seeded X-ray free-electron laser covering the 3.5 keV to 14.6 keV range, Nat. Photonics **15**, 435, 2021.

[13] K.-J. Kim, Y. Shvyd'ko, and S. Reiche, A proposal for an x-ray free-electron laser oscillator with an energy-recovery linac, Phys. Rev. Lett. **100**, 244802 (2008).

[14] K.-J. Kim and Y. V. Shvyd'ko, Tunable optical cavity for an x-ray free-electron-laser oscillator, Phys. Rev. ST Accel. Beams **12**, 030703 (2009).

[15] R. R. Lindberg, K.-J. Kim, Yu. Shvyd'ko, and W. M. Fawley, Performance of the x-ray free-electron laser oscillator with crystal cavity, Phys. Rev. ST Accel. Beams **14**, 010701 (2011).

[16] Z. Huang and R. D. Ruth, Fully coherent x-ray pulses from a regenerative-amplifier free-electron laser, Phys. Rev. Lett. **96**, 144801 (2006).

[17] H. P. Freund, P. J. M. van der Slot, and Yu. Shvyd'ko, An x-ray regenerative amplifier free-electron laser using diamond pinhole mirrors, New J. Phys. **21**, 093028 (2019).

[18] G. Marcus, A. Halavanau, Z. Huang, J. Krzywinski, J. MacArthur, R. Margraf, T. Raubenheimer, and D. Zhu, Refractive guide switching a regenerative amplifier free-electron laser for high peak and average power hard x rays, Phys. Rev. Lett. **125**, 254801 (2020).

[19] P. Qi and Yu. Shvyd'ko, Signatures of misalignment in x-ray cavities of cavity-based x-ray free-electron lasers, Phys. Rev. Accel. Beams **25**, 050701 (2022).

[20] G. Marcus, J. Anton, L. Assoufid, F.-J. Decker, G. Gassner, K. Goetze, A. Halavanau, J. Hastings, Z. Huang, W. Jansma *et al.*, Cavity-based free-electron laser research and development: A Joint Argonne National Laboratory and SLAC National Laboratory collaboration, in *Proceedings of the 39th International Free Electron Laser Conference* (JACoW, Geneva, Switzerland, 2019), 10.18429/JACoW-FEL2019-TUD04.

[21] F.-J. Decker, K. Bane, W. Colocho, A. Lutman, and J. Sheppard, Recent developments and plans for two bunch operation with up to 1 μs separation at LCLS, in *Proceedings of the 38th International Free Electron Laser Conference, Santa Fe* (JACoW, Geneva, Switzerland, 2017), 10.18429/JACoW-FEL2017-TUP023.

[22] K.-J. Kim, L. Assoufid, R. R. Lindberg, X. Shi, D. Shu, Yu. Shvyd'ko, M. White, F.-J. Decker, Z. Huang, G. Marcus *et al.*, Test of an X-ray cavity using double-bunches from the LCLS Cu-linac, in *Proceedings of the 10th International Particle Accelerator Conference, Melbourne, Australia* (JACoW, Geneva, Switzerland, 2019), 10.18429/JACoW-IPAC2019-TUPRB096.

[23] P. Liu, P. Pradhan, X. Shi, D. Shu, K. Kauchha, Z. Qiao, K. Tamasaku, T. Osaka, D. Zhu, T. Sato *et al.*, Design, fabrication, and characterization of x-ray optics for the cavity-based x-ray free-electron laser project, edited by L. Assoufid, H. Ohashi, and F. Siewert, in *Advances in Metrology for X-Ray and EUV Optics X* (SPIE, Bellingham, 2023), Vol. 12695, p. 126950C, 10.1117/12.2677194.

[24] P. Liu, P. Pradhan, X. Shi, D. Shu, K. Kauchha, Z. Qiao, K. Tamasaku, T. Osaka, D. Zhu, T. Sato, J. MacArthur, X. Huang, L. Assoufid, M. White, K.-J. Kim, and Y. Shvyd'ko, X-ray optics for the cavity-based X-ray free-electron laser, J. Synchrotron Radiat. **31**, 751 (2024).

[25] T. Kolodziej, P. Vodnala, S. Terentyev, V. Blank, and Yu. Shvyd'ko, Diamond drumhead crystals for X-ray optics applications, J. Appl. Crystallogr. **49**, 1240 (2016).

[26] Yu. Shvyd'ko, Output coupling from x-ray free-electron laser cavities with intracavity beam splitters, Phys. Rev. Accel. Beams **22**, 100703 (2019).

[27] K. Li, Y. Liu, M. Seaberg, M. Chollet, T. M. Weiss, and A. Sakdinawat, Wavefront preserving and high efficiency diamond grating beam splitter for x-ray free electron laser, Opt. Express **28**, 10939 (2020).

[28] P. Liu, P. Pradhan, A. Miceli, D. A. Walko, D. Shu, J. Sullivan, K. Lang, M. Rivers, D. Zhu, A. Halavanau, and Y. Shvyd'ko, Design and characterization of x-ray diagnostics for the cavity-based x-ray free-electron laser project, in *Advances in X-Ray/EUV Optics and Components XVIII*, edited by H. Mimura, A. M. Khounsary, and C. Morawe (International Society for Optics and Photonics, SPIE, 2023), Vol. 12694, p. 126940D, 10.1117/12.2677209.

[29] X. Shi, Z. Qiao, P. Pradhan, P. Liu, L. Assoufid, K.-J. Kim, and Y. Shvyd'ko, At-wavelength characterization of X-ray wavefronts in Bragg diffraction from crystals, J. Synchrotron Radiat. **30**, 1100 (2023).

[30] Yu. Shvyd'ko, Theory of angular-dispersive, imaging hard-x-ray spectrographs, Phys. Rev. A **91**, 053817 (2015).

[31] K. Kauchha, P. Liu, P. Pradhan, and Y. Shvyd'ko, Single-shot meV-resolution hard X-ray spectrograph for CBXFEL diagnostics, in *Proceedings of the 15th International Particle Accelerator Conference, IPAC-2024, Nashville, TN* (2024), p. TUPG04, unpublished.

[32] M. Balcazar *et al.*, LCLS Technical Note Report No. LCLS-II-TN-24-02. G. Marcus (SLAC) and K.-J. Kim (ANL) are acknowledged for providing simulated photon numbers for XRAFEL and XFELO cases.

[33] A. Koch, C. Raven, P. Spanne, and A. Snigirev, X-ray imaging with submicrometer resolution employing transparent luminescent screens, J. Opt. Soc. Am. A **15**, 1940 (1998).

[34] K. Tono, T. Togashi, Y. Inubushi, T. Sato, T. Katayama, K. Ogawa, H. Ohashi, H. Kimura, S. Takahashi, K. Takeshita *et al.*, Beamline, experimental stations and photon beam diagnostics for the hard x-ray free electron laser of SACLA, New J. Phys. **15**, 083035 (2013).

[35] A. Koch, W. Freund, J. Grünert, M. Planas, T. Roth, L. Samoylova, and V. Lyamayev, Design and initial characterisation of X-ray beam diagnostic imagers for the European XFEL, in *Advances in X-ray Free-Electron Lasers Instrumentation III*, edited by Sandra G. Biedron (International Society for Optics and Photonics, SPIE, 2015), Vol. 9512, p. 291–302.

[36] A. Koch, J. Risch, W. Freund, T. Maltezopoulos, M. Planas, and J. Grünert, Operation of photon diagnostic imagers for beam commissioning at the European XFEL, J. Synchrotron Radiat. **26**, 1489 (2019).

[37] A. Gottwald, U. Kroth, M. Krumrey, M. Richter, F. Scholze, and G. Ulm, The PTB high-accuracy spectral responsivity scale in the VUV and x-ray range, Metrologia **43**, S125 (2006).

[38] R. C. Burns, A. I. Chumakov, S. H. Connell, D. Dube, H. P. Godfried, J. O. Hansen, J. H. ärtwig, J. Hoszowska, F. Masiello, L. Mkhonza, M. Rebak, A. Rommevaux, R. Setshedi, and P. Van Vaerenbergh, HPHT growth and x-ray characterization of high-quality type IIa diamond, J. Phys. Condens. Matter **21**, 364224 (2009).

[39] H. Sumiya and K. Tamasaku, Large defect-free synthetic type IIa diamond crystals synthesized via high pressure and high temperature, Jpn. J. Appl. Phys. **51**, 090102 (2012).

[40] R. Margraf, R. Robles, A. Halavanau, J. Krzywinski, K. Li, J. MacArthur, T. Osaka, A. Sakdinawat, T. Sato, Y. Sun *et al.*, Low-loss stable storage of x-ray free electron laser pulses in a 14 m rectangular Bragg cavity, Nat. Photonics **17**, 878 (2023).

[41] A. Macrander, M. Erdmann, N. Kujala, S. Stoupin, S. Marathe, X. Shi, M. Wojcik, D. Nocher, R. Conley, J. Sullivan *et al.*, X-ray optics testing beamline 1-BM at the Advanced Photon Source, AIP Conf. Proc. **1741**, 030030 (2016).

[42] D. A. Walko, B. W. Adams, G. Doumy, E. M. Dufresne, Y. Li, A. M. March, A. R. Sandy, J. Wang, H. Wen, and Y. Zhu, Developments in time-resolved x-ray research at APS beamline 7ID, AIP Conf. Proc. **1741**, 030048 (2016).

[43] J. Bohon, E. Muller, and J. Smedley, Development of diamond-based X-ray detection for high-flux beamline diagnostics, J. Synchrotron Radiat., **17**, 711 (2010).

[44] J. Bohon, E. Gonzalez, C. Grace, C. T. Harris, B. Jacobsen, S. Kachiguine, D. Kim, J. MacArthur, F. Martinez-McKinney, S. Mazza *et al.*, Use of diamond sensors for a high-flux, high-rate x-ray pass-through diagnostic, J. Synchrotron Radiat. **29**, 595 (2022).